Glass structure of industrial ground granulated blast furnace slags (GGBS) investigated by time-resolved Raman and NMR spectroscopies

Simon Blotevogel, Valérie Montouillout, Aurélien Canizares, Patrick Simon, Erwan Chesneau, Abel Danezan, Thomas Wattez, Andreas Ehrenberg, Mathilde Poirier, Cédric Patapy, et al.

Glass structure of industrial ground granulated blast furnace slags (GGBS) investigated by time-resolved Raman and NMR spectroscopies

Simon Blotevogel[1], Valérie Montouillout[2], Aurélien Canizares[2], Patrick Simon[2], Erwan Chesneau[2], Abel Danezan[2], Thomas Wattez[3], Andreas Ehrenberg[4], Mathilde Poirier[1,3], Cédric Patapy[1], Martin Cyr[1]

1 LMDC, Université de Toulouse, INSA/UPS Génie Civil, 135 Avenue de Rangueil, 31077, Toulouse cedex 04, France

2 Conditions Extrêmes et Matériaux: Haute Température et Irradiation CEMHTI, CNRS UPR 3079, Univ. d'Orléans 1D Avenue de la Recherche Scientifique, F-45071 Orléans Cedex 2, France

3 Ecocem Materials, 324061, Block F1, Eastpoint Business Park, Dublin 3, Ireland

4 Institut Für Baustoff-Forschung e.V. (FEHS), Bliersheimer Str.62, 47229 Duisburg, Germany

Abstract

Ground granulated blast furnace slags (GGBS) are glassy by-products from iron production that are commonly used as supplementary cementitious materials in blended cements. The glass structure of seven industrial GGBS was investigated by Raman and Nuclear Magnetic Resonance spectroscopies. The complex composition of the slags induced multiple analytical challenges. Under usual continuous excitation, the Raman signal was masked by strong luminescence, so that analysis was carried out on a time-resolved Raman (TRR) device. TRR allowed to eliminate luminescence and resulted in exploitable spectra that showed variations in line with theoretical NBO/T values. The analysis of ^{27}Al and ^{29}Si NMR spectra was complicated by the presence of paramagnetic nuclei and the wide variety of environments. Nevertheless, ^{27}Al NMR showed that Al was present as a network former, mainly in 4-fold coordination and careful analyses of ^{29}Si NMR spectra allowed the comparison of glass network polymerization of industrial GGBS in line with the theoretical NBO/T based on their composition.

This manuscript was published in the Journal of Materials Science under doi: 10.1007/s10853-021-06446-4

1. Introduction

Ground granulated blast furnace slag (GGBS) is a glassy by-product of hot metal production and has been used in blended cements for over 140 years [1–4]. GGBS-containing binders and concretes have a lower CO_2 footprint, show a decreased heat development and an increased physical and chemical resistance [1, 3, 5–8]. At high replacement levels, the short term compressive strength of GGBS is below that of ordinary Portland cement (OPC), but there are large differences between different GGBS [1–4, 7, 9–13].

The main source of variation in GGBS reactivity in various cementitious systems are differences in their chemical composition [11, 12, 14–19]. During the hydration reaction of blended cements, the slag glass dissolves in an alkaline aqueous medium (pH ≈12-13, due to the presence of cement or an alkaline activator). Subsequently typical cementitious phases as C-(A)-S-H, hydrotalcite, AFm and ettringite precipitate and give mechanical-strength to the material [1, 3, 12]. Consequently, the observed differences in reactivity are likely due to differences in chemical durability of the slag glass, which in turn is strongly dependent on the polymerization degree of the Si-network [3, 20].

GGBS are calcium aluminosilicate glasses, also containing some MgO and even less TiO_2 in the order of a few wt.%, and a wide variety of other elements in amounts below the wt. % [1, 2, 12]. Generally, GGBS containing higher proportions of CaO and MgO with respect to SiO_2 are more reactive, independently of the activation system [12, 15, 17, 18]. This underlines the link between reactivity and the degree of polymerization of the vitreous network of GGBS. The role of Al is more complex as, in the presence of OPC, high Al containing slags also showed good short term (< 2-days) performances, even though Al is expected to stabilize the glass network [12, 20, 21].

For a wide compositional range of aluminosilicate glasses, both Si and Al are tetrahedrally coordinated with oxygen and considered as network formers. Each of these tetrahedral units can share corners with other tetrahedra through bridging oxygens (BO), thus giving the glass network different degrees of polymerization [21–23]. However, in contrast to SiO_4 units, AlO_4^-

tetrahedra require a charge-compensation easily achieved in the case of GGBS by the presence of Na^+, K^+, Ca^{2+} and Mg^{2+}, considered then as charge compensators [24–27]. All of the alkaline and a part of alkaline-earth cations are therefore requisitioned for charge compensation. The remaining alkaline-earth cations are responsible of network depolymerisation by forming non-bridging oxygens (NBO) and are then called network modifiers.

The polymerization of the glass network is conventionally described using the Q^n notation, i.e., the connectivity of its tetrahedra. In this notation, n represents the number of BOs per tetrahedron: Q^0 corresponds to an isolated tetrahedron and Q^4 corresponds a fully polymerized tetrahedron. By assuming a certain structural role for each element, it is possible to estimate an average NBO/tetrahedron based on the glass composition and the charge equilibrium of the system. This value gives an overall estimate of the polymerization state of the glass. However it does not take into account the presence of structural heterogeneities, such as lower polymerized domains, which can play essential roles in GGBS dissolution [28, 29]. Therefore, an experimental evaluation of the slag glass structure is necessary.

Conventional Raman spectroscopy was extensively used to investigate the structure of silicate glasses. Initially, it was used to study the effect of different elements on the glass network formation in relatively simple model glasses [30–36]. Recently, some studies attempted to approach GGBS glass compositions using synthesized CaO-SiO_2 glasses adding various quantities of TiO_2, Al_2O_3 and MgO [37–39]. The latter studies provided insights on modification of the glass structure due to CaO, Al_2O_3 and TiO_2 content modification. Only one study attempted to approach real slag glass conditions by synthesizing their samples based on the vitrification of air pollution control residues [40]. The absence of Raman studies of real, industrial slag glasses is likely due to luminescence of transition metals in complex glasses [41]. By using the noticeably different emission times of Raman and luminescence after a laser pulse, the use of time-resolved Raman spectroscopy can avoid those difficulties [42, 43].

Similarly, solid state Nuclear Magnetic Resonance (NMR) spectroscopy is an essential technique for the structural characterization of vitreous networks. The literature is very abundant in the aluminosilicate domain and the effect of the different modifiers (alkaline, alkaline earth, or rare

earth) has been widely explored [44, 45]. Several isotopes are easily observable as ^{29}Si, ^{27}Al, ^{23}Na, others need isotopic enrichment (^{17}O, ^{43}Ca, ^{25}Mg, ...). NMR allows detailed description of the network of glasses with similar main oxide composition as GGBS. However, the study of real GGBS is made very difficult by the presence of numerous atoms and especially paramagnetic elements as Fe^{3+}, Mn^{4+}, Cr^{3+}, etc, preventing unambiguous quantitative spectral analyses. Moreover, the isotope enrichment of industrial slags is obviously unachievable, preventing the use of correlation experiments and isotopes with low natural abundance such as ^{43}Ca.

In the present study, the glass structure of seven industrial GGBS was investigated by ^{29}Si and ^{27}Al NMR and time-resolved Raman spectroscopies. Because GGBS are glasses with relatively complex compositions, various analytical problems had to be overcome. By optimizing the spectra acquisition and treatment, and analyzing the results with the necessary perspective on the limitations of each technique, we aimed to gain insights on the local structure of the slag glasses and the topology of network formers.

2. Materials and Methods

2.1 Materials

For the investigation of their glass structure, seven GGBS were selected from the 16 GGBS presented in [12] (Table 1). The sample numbers from the reference were kept to allow identification of the different samples. All seven GGBS are modern industrial slags from Europe and were chosen to represent a wide range of reactivity and composition. In mortar strength tests according to EN 196-1, the 2-day compressive strength was shown to be most dependent on GGBS reactivity [12]. The selected samples showed a 2-day compressive strength between 4.3 MPa and 15.6 MPa, covering almost the entire range of reactivity reported in [12]. All GGBS were considered as almost totally amorphous, with glass content > 99.8%, except for GGBS 14 with a glass content of 98.2% and GGBS13 with 2.6 wt.% of akermanite, detected by Q-XRD [12].

The GGBS composition was determined on fused tabs by XRF (Panalytical Zetium) [12]. CaO contents in our dataset were between 33.9 and 43.2 wt. %, with an average of 40.1 wt.%. SiO_2 contents in our GGBS set range from 34.6 to 39.2 wt. %, a distribution that is on both ends about 2 wt.% smaller than the extreme values for GGBS from different regions of the world reported in Matthes et al. (2018) [1]. For Al_2O_3 the observed concentration range between 9.6 to 13.7 wt.%. MgO contents in our sample set are between 6.4 and 10.4 wt.%. In the studied GGBS, TiO_2 contents range for 0.43 to 3.02 wt. %. This range corresponds to the full range observed by Matthes et al. (2018) [1]. Comparable data for Na_2O and K_2O are not published, mostly due to the use of Na_2O equivalent measures in cement industry. Na_2O equivalent values are reported to be between 0.18 and 1.94 wt.% [11].

Table 1. Chemical composition of the studied slags and results of compressive strength tests according to EN 196-1, on 75% GGBS, 25% clinker in standard mortars. This data is part of the data published in [12]**. Mean values and relative standard deviation (RSD, in %) are given for all parameters.**

ID	CaO	SiO_2	Al_2O_3	MgO	TiO_2	Na_2O	K_2O	2 d	28 d
	wt.-%	wt.-%	wt.-%	wt.-%	wt.-%	wt.%	wt.%	MPa	MPa
GGBS 2	42.0	36.6	12.0	6.94	0.74	0.42	0.53	11.2	47.5
GGBS 3	40.9	37.6	9.61	6.40	0.61	0.38	0.36	8.2	48.5
GGBS 9	39.5	37.4	11.0	6.64	3.02	0.41	0.44	4.3	37.9
GGBS 11	43.2	36.3	11.8	6.30	0.43	0.41	0.25	15.6	54.3
GGBS 12	42.0	36.8	11.7	6.60	0.70	0.61	0.57	10.6	50.6
GGBS 13	33.9	39.2	11.2	10.4	0.57	0.45	1.51	5.1	44.6
GGBS 14	38.9	34.6	13.7	8.36	1.16	0.39	0.44	14.8	49.2
Mean	40.1	36.9	11.6	7.4	1.0	0.44	0.59	10.0	47.5
RSD (%)	7.7	3.8	10.6	20.4	87.7	17.8	71.9	44.1	10.9

2.2 Methods

2.2.1 Continuous Raman spectroscopy

First tests were carried out on two conventional Raman spectrometers (InVia Reflex and InVia Qontor Renishaw) using classical continuous lasers for sample excitation at different wavelengths (355, 514, 633 and 785 nm). All spectra showed strong luminescence effects (Figure 1) that completely masked the relevant Raman information. Usually, by using such a large range of excitation lines from IR to UV, at least one of them allows satisfactory acquisition of Raman spectra. Because of the high concentration of impurities such as transition metals in these industrial products, luminescence could not be eliminated by shifting the excitation line out of the absorption bands. The observed effects likely explain why no Raman spectra of industrial GGBS are reported in literature and that the published studies work on model glasses with diluted transition metal content [37]. To avoid luminescence, this study was performed on a time-resolved Raman device, allowing to separate Raman scattering from luminescence owing to their different emission times.

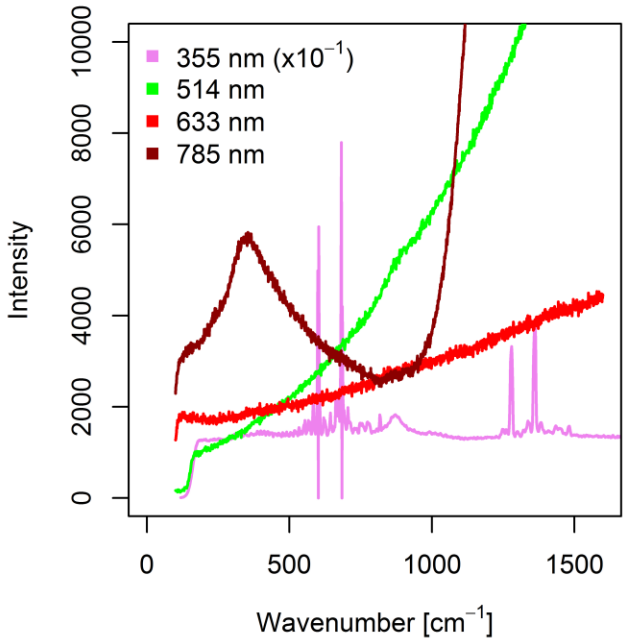

Figure 1. Raman spectra of a GGBS sample excited by different continuous laser wavelengths. For all wavelengths, high luminescence effects mask Raman scattering.

2.2.2 Time resolved Raman spectroscopy

TRR measurements were carried out on GGBS powders, that were pressed into small pellets (around 3 mm of diameter) using a hand operated pelletizer. Two spectra were measured on two different spots on each pellet.

A Jobin-Yvon T64000 triple spectrometer, with substractive configuration, equipped with three 1800 grooves mm^{-1} gratings, in the backscattering mode, was used. The microscope was an Olympus BX40 (objective 10×, NA=0.25). This time-resolved Raman spectrometer was equipped with a frequency-doubled Nd^{3+}: YAG pulsed laser (by Spectra-Physics FCBar T40-X30) to excite samples. Emitted wavelength was 532 nm (linewidth 1 cm^{-1}), with a pulse width of about 30–50 ns, cycled every milllisecond. This spectrometer (CNRS CEMHTI laboratory, Orléans) has been described in detail elsewhere [42, 43, 46].

Raman scattering was detected by an ICCD (Intensified CCD, DH 720, Andor Technology) and its detector gate was triggered by the electronic command of the Q-switch of the laser cavity, through a pulse/delay generator. Thus, every point in time, i.e., before, during and after the

laser pulse, can be measured. The Raman effect is much quicker than the nanosecond range, and is virtually simultaneous to the laser pulse at this time scale. The main part of luminescence is emitted later. In this study, the detector gate was opened simultaneously to the laser pulse (0 delay, same width).

2.2.3 Raman data processing

An average spectrum of five measurements (5s accumulation time each) was computed for each sample. Then, the black current measurement and a quadratic baseline were subtracted from each Raman spectrum. Defect pixels in the range of 1051 cm^{-1} and 1083 cm^{-1} were corrected by linear interpolation between these points. Average spectra from the two measurements on each sample are displayed in Figure 2a.

To interpret the Raman spectra, different bands were fitted into the measured envelop. Therefore, spectra were normalized to maximum height = 1 and fitted using six gaussian curves. In a first fitting step, peak positions were set to be in ranges from 670-720 cm^{-1} for the first Ti-O-Si band, 770-810 cm^{-1} for the second Ti-O-Si band, 850-865 cm^{-1} for the Q^0 band, 900-912 cm^{-1} for the Q^1 band, 950-1000 cm^{-1} for the Q^2 band and 1000-1100 cm^{-1} for the Q^3 band, according to literature [39, 47]. Peak position, height and width were then fitted. In a second fitting step, peak positions were fixed to 689 cm^{-1}, 779 cm^{-1}, 854 cm^{-1}, 910 cm^{-1}, 960 cm^{-1} and 1010 cm^{-1}. These positions were either derived from discernable shoulders on the fitted spectra or, where not applicable, mean values from the first fitting step. The ratio of the areas of Q^0 and Q^2 units was computed to quantify the degree of polymerization of the glass network. This ratio was chosen to oppose the most and least polymerized structural units that were well resolved in Raman spectra deconvolution.

2.2.4 **NMR**

For NMR measurements powdered GGBS samples were put into a rotor. The ^{29}Si MAS NMR spectra were acquired on a Bruker Avance I 400 MHz (static magnetic field B_0=9.4 T) operating

at a Larmor frequency of ν_0 (^{29}Si) = 79.4 MHz, using a 4mm probe and with a spinning rate of 10 kHz. Each spectrum necessitated the sum of 2000 to 4000 transients accumulated with a recycling delay of 60 s insuring complete relaxation of the magnetization (total acquisition time between 24 and 48 hours). Chemical shifts are given relative to tetramethylsilane (TMS) at 0 ppm.

^{27}Al MAS NMR spectra were collected on a Bruker Avance III 850 MHz (B_0=20.0 T) spectrometer operating at ν_0 (^{27}Al) = 221.6 MHz equipped with high speed MAS probe heads (spinning rate of 30 kHz using aluminum-free zirconia rotors of 2.5 mm diameter). Each 1D MAS spectra necessitated the sum of 2048 to 4096 transients accumulated using a $\pi/18$ pulse and a recycle time of 1 s to assure a quantitative signal (total acquisition time of around 1 hour). Chemical shifts were reported to 0 ppm with respect to $Al(NO_3)_3$ 1 molar aqueous solution.

2.2.5 NMR data processing

All Free Induction Decays (FID) recorded were processed by a homemade Python code using Nmrglue and NumPy librairies [48, 49] and Topspin software. A Gaussian apodization was applied with a broadening 100 Hz for ^{29}Si and ^{27}Al data, followed by a fast Fourier transform and zero and first-order phase correction. Special care has been applied to first order phase determination for the broad featureless ^{29}Si spectra, taking into account in particular the pre scan delay (DE). For both ^{29}Si and ^{27}Al spectra, a baseline correction was applied subtracting a polynomial function of degree 4 and 16 for ^{29}Si and ^{27}Al spectra, respectively.

The position of the center of gravity of ^{29}Si spectra was determined as the position of the half of the full integral in the range -40 to -120ppm. Likewise, full width at half maximum is determined as the distance, in ppm, between two points where the intensity is equal the half of the maximum intensity in the same range than for the center of gravity. The deconvolution of

^{27}Al NMR spectra was carried out using DM-FIT [50] software, using CzSimple model lines deduced from the GIM (Gaussian Isotropic Model) model [51].

3. Results

3.1 Raman spectroscopy

3.1.1 Spectra description

Time-resolved Raman spectra of all slag glasses presented a broad envelop with maximum values around 880 cm^{-1} (Figure 2a). The envelope corresponded to the range of asymmetric and symmetric stretching of Si-O, representing different connectivities of SiO_4 units in the glass network [30, 47, 52]. Raman bands of SiO_4 units depend on their connectivity, ranging from 850 cm^{-1} for isolated SiO_4 (Q^0) units to fully connected Q^4 units between 1060 and 1200 cm^{-1} [47]. Typical ranges of the Raman bands are indicated by the colored background in Figure 2 [47, 52]. The main intensity of slag glass spectra in this study was detected between the wavenumbers attributed to Q^0 and Q^1 bands.

Besides the main envelop of Si-O vibrations, a broad band just before the typical Si tetrahedron range was detected in all spectra with variable intensity. Several bands in this area were attributed to Ti-O-Si vibrations in TiO_2-CaO-SiO_2 glasses and slags [39]. However, other studies attribute peaks in this region to Si-O motions and one study found variation of bands with Al content of Na_2O-Al_2O_3-SiO_2 glasses [53–56].

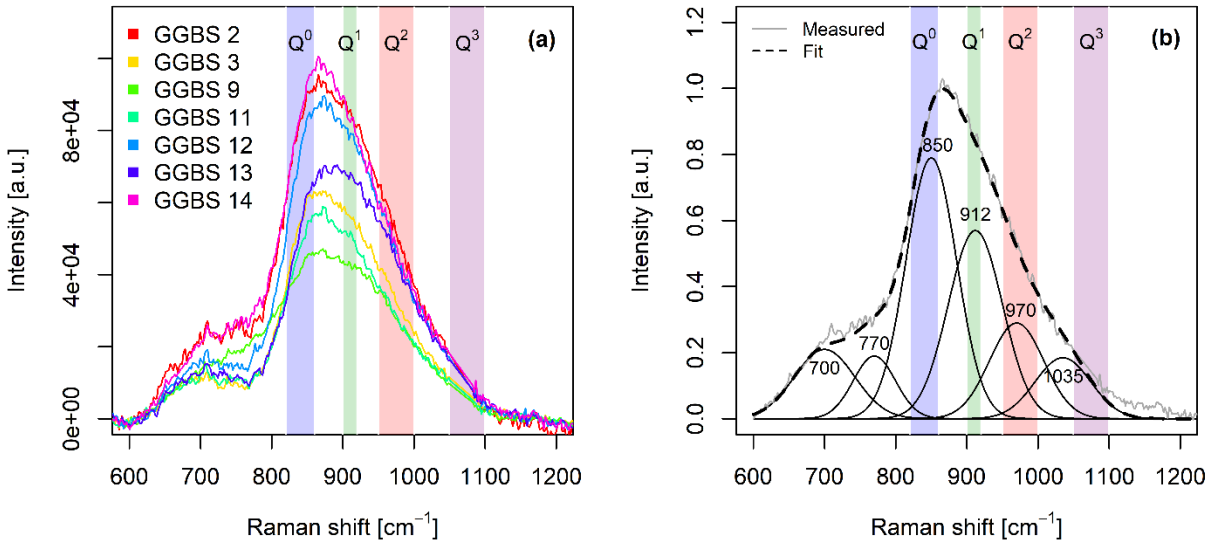

Figure 2. (a) Average time-resolved Raman spectra of the seven investigated GGBS. (b) Fit of GGBS14 spectrum. Colored rectangles indicate Raman bands of Q^0 to Q^4 units of Si tetrahedra (after Mysen et al. 1980 and McMillan 1984 [47, 52]**).**

3.1.2 Deconvolution of Raman spectra

Deconvolution of the spectra showed changes in the relative intensity of the different bands, thereby indicating differences in the polymerization of the glass network (Figure 2b/Table 2). Some studies derive an actual NBO/T from deconvolution data [39]. This was attempted, but the first results were strongly depending on small changes in Q^3 band. As the position of the Q^3 band is known to shift with differences glass compositions, the calculated NBO/T values were highly dependend on deconvolution parameters [57]. In consequence, the ratio of Q^0/Q^2 convoluted areas was chosen as a more robust measure of network polymerization.

The highest ratio of the deconvoluted area of Q^0/Q^2 bands and thus the highest depolymerization of the Si network was calculated for GGBS3 and GGBS14, with a ratio of 2.64 and 2.54, respectively. Lowest ratios were calculated for GGBS13 and GGBS9 (1.45 and 1.90, respectively). Globally, the glass network connectivity, as indicated by the Q^0/Q^2 ratio, was decreasing in the following order GGBS 13 > GGBS 9 > GGBS 2 > GGBS 12 > GGBS 11 > GGB 14 >

GGBS3 (Table 2). However, keep in mind that those numbers do not correspond to real Q^0/Q^2 structural unit ratios, as vibrational modes of Q^0 and Q^2 units have not the same Raman scattering cross-section owing to their different polarizability [58]. This means that the Q0/Q2 values show relative changes in polymerization not absolute abundances.

The attribution of the band at 770 cm^{-1} to Ti-O-Si vibrations can be confirmed as GGBS 9, with the highest TiO_2 content (3.02 wt%), had the largest area for this band. The attribution of the 700 cm^{-1} band to Ti-O-Si vibration suggested in literature, appeared not to be plausible, as only small changes were observed between the samples [59]. In earlier literature on binary glasses, a band at around 700 cm^{-1} was attributed to Q^1, pyrosilicate like dimer units [60]. However, deconvoluted band areas between Q^1 and units at 912 cm^{-1} and the 700 cm^{-1} band did not vary analogously. Furthermore the variation could not be explained by variations in Al_2O_3 content of the glass as could be expected from [53]. Likely, multiple structural units contribute to this band, so that it was not possible to assign it unambiguously.

3.2 Solid state NMR

The ^{29}Si NMR spectra of the different samples, all exhibiting a single broad signal, are shown on Figure 3a. The first obvious observation is that all spectra have a similar lineshape, except GGBS13 one which presents a Lorentzian-like resonance spanning more than 80 ppm : this specific lineshape is due to the presence of paramagnetic nuclei, especially Mn^{4+} (1.290.77 wt% of Mn) interacting with ^{29}Si. In all the other GGBS, the signal was rather Gaussian-like, centered at around 75 ppm, spreading from -65 to -90 ppm. These lineshapes and their width resulted from the chemical shift distribution due to the wide panel of silicon environments in the slag glass network.

Table 2. Deconvoluted band areas (arbitrary units) assigned to different tetrahedron connectivities and Ti-O-Si vibrations. The Q^0/Q^2 ratio is given as an indicator of glass network polymerization.

ID	Q^3	Q^2	Q^1	Q^0	Ti-O-Si	ND	Q^0/Q^2

	(1035 cm^{-1})	(970 cm^{-1})	(912 cm^{-1})	(850 cm^{-1})	(770 cm^{-1})	(700 cm^{-1})	
GGBS2	18	32	60	69	16	24	2.19
GGBS3	22	26	62	70	6	21	2.64
GGBS9	22	38	59	73	33	27	1.90
GGBS11	17	29	57	66	7	21	2.28
GGBS12	20	30	62	66	7	21	2.21
GGBS13	23	36	74	53	9	21	1.45
GGBS14	18	28	55	71	14	22	2.54

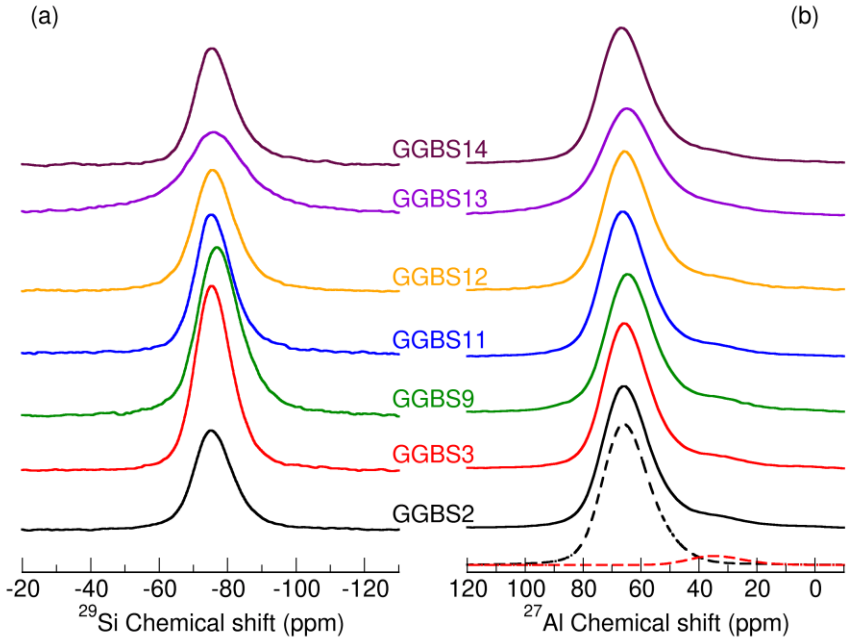

Figure 3: (a) ^{29}Si MAS NMR spectra at 9.4 T with a spinning rate of 10 kHz; (b) ^{27}Al MAS NMR spectra at 20.0 T with a spinning rate of 30 kHz of seven investigated GGBS. All spectra were normalized with full integral equal to 1.

The position of the center of gravities (δ_{CG}) and the full width at half maximum (FWHM) of the different signals are shown in Table 3. The δ_{CG} values differ only slightly from one sample to the other, and are located in the range of Q^1 and Q^2 units [61]. Only for GGBS9 and GGBS14, δ_{CG} was

more negative. Moreover, FWHM presented only small differences, except for GGBS13. This was due to the presence of a paramagnetic interaction, as previously indicated.

Table 3 –Position of the center of gravity and FWHM of ^{29}Si NMR signals. The uncertainties are estimated to ±0.1ppm, and ±5Hz respectively

	δ_{CG} (ppm)	FWHM (Hz)
GGBS2	-76.7	1035
GGBS3	-76.7	998
GGBS9	-78.4	1178
GGBS11	-76.7	1007
GGBS12	-76.9	1117
GGBS13	-76.4	1596
GGBS14	-77.9	1051

^{27}Al NMR spectra are shown in Figure 3(b). As observed on ^{29}Si NMR spectra, the signal of GGBS13 differs from the others by its lineshape and width. This is again due to the paramagnetic interaction with Mn^{4+}. All other spectra exhibit very similar features, with a main signal centered at around 65 ppm and a smaller shoulder at 35 ppm. The resonance exhibits a quadrupolar lineshape characteristic of disordered materials, with a broad asymmetric lineshape. The main signal is associated with the presence of aluminum in four-fold coordination and the smaller shoulder is consistent with five-fold coordinated aluminum [36, 62]. In the case of GGBS13, the paramagnetic Lorentzian broadening prevent the clear distinction of Al_{IV} and Al_V species.

The NMR parameters, as well as the relative quantity of four-fold and five-fold coordinated aluminum derived from deconvolution of the spectra, are presented in Table 4.

Table 4 – Isotropic chemical shift, mean quadrupolar coupling constant and proportion of Al species obtained from the ^{27}Al NMR analysis. The uncertainties are estimated to ±0.5ppm, ±0.1kHz and ±1% respectively.

	Al_{IV}			Al_V		
	δ_{iso}(ppm)	C_Q(MHz)	%	δ_{iso}(ppm)	C_Q(MHz)	%

GBS2	73.2	8.0	95	39.1	8.0	5
GBS3	72.4	7.9	93	39.5	7.4	7
GBS9	71.5	7.9	93	38.7	7.9	7
GBS11	73.3	8.0	95	39.2	8.0	5
GBS12	72.4	7.9	94	39.9	7.9	6
GBS13	68.8	6.6	98	38.2	7.4	2
GBS14	72.5	7.4	98	38.2	7.4	2

In all cases, a majority of the intensity (93 to 98 %) was assigned to the tetrahedral environment. The chemical shifts of the corresponding signal range from 71.5 ppm to 73.3 ppm. The difference of values obtained for GGBS13 may be related to the Lorentzian broadening, which renders an accurate simulation difficult. The measured chemical shifts were unexpectedly high compared to literature data for glasses with similar main oxide composition (around 68 ppm) [25-26]. This difference might be due to the presence of NBOs on aluminum tetrahedra. The measured C_Q values are in good agreement with the presence of alkaline earth cations as charge compensators [25-26]. The five-fold coordinated aluminum quantities appeared very close (and very low) in all samples.

4. Discussion

4.1 Theoretical description of the GGBS vitreous network

The computation of a theoretical NBO/T needs assumptions on the role of each element in the glass structure. The assignment of Si as a 4-fold coordinated network former and Ca, Mg, K and Na as network modifiers is obvious from literature [21, 63, 64]. In contrast, Al can be present in different coordination environments leading to different roles in the glass network [25, 62].

The ^{27}Al NMR spectra of all GGBS showed that the vast majority of aluminum of our systems is in tetrahedral coordination to oxygen, playing the role of network former. This observation is in line with former literature on slag like model glasses [21]. The negative charge induced by the presence of these AlO_4^- is compensated by the positive charge of either Na^+, K^+, Ca^{2+} or Mg^{2+}. In this context, assuming the complete charge compensation in the network, it is possible to

estimate a mean NBO per tetrahedron using Eq 1. Note that in the equation n corresponds to the mole number of each element.

$$\frac{NBO}{T} = \frac{n_{Na} + n_K + 2n_{Ca} + 2n_{Mg} - n_{Al}}{n_{Si} + n_{Al}} \qquad \text{(Eq. 1)}$$

Table 5. Theoretical NBO/T values derived from GGBS compositions using Eq. 1. Al/Si values are molar ratios of the two main network formers.

	NBO/T	Al/Si
GGBS2	1.93	0.39
GGBS3	1.98	0.30
GGBS9	1.83	0.35
GGBS11	1.96	0.38
GGBS12	1.93	0.37
GGBS13	1.78	0.34
GGBS14	1.84	0.47

Applying this equation to the composition of the studied slags yields the theoretical NBO/T values in Table 5. For the seven industrial slags, the theoretical NBO/T ranges from 1.78 to 1.98. Obviously this calculation is simplistic as it neglects all other potential network formers (Fe^{3+}, Ti^{4+}, …), and assumes an equivalent distribution of NBO on Si and Al tetrahedra. Recently, Le Cornec et al. [65] estimated a slightly different repartition of NBO on Si (on average $Q^{2.06}$) and Al (on average $Q^{2.67}$) on GGBS. Nevertheless, Eq. 1 takes into account the main oxides and gives a good estimate of the polymerization degree of the glass network.

4.2 Evaluation of slag structure by time-resolved Raman spectroscopy

Theoretical NBO/T and Q^0/Q^2 from Raman spectra follow the same trend (Figure 4). Linear regression between NBO/T and Q^0/Q^2 ratios gave an R^2 of 0.50. The only sample significantly deriving from this trend is GGBS14. Exclusion of this sample from the regression leads to an improved R^2 of 0.92. This demonstrates that except for the sample with the highest Al content,

time-resolved Raman spectra deconvolution is sensitive to variations in the Si glass network polymerization in complex slag glasses.

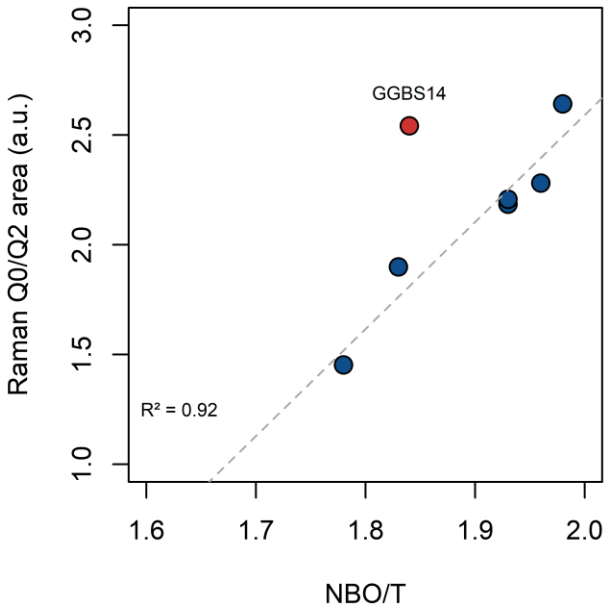

Figure 4. Experimental Raman Q^0/Q^2 area ratio plotted against theoretical NBO/T. The dotted line represents a linear regression, excluding GGBS14.

The main difference of GGBS14 with respect to the other samples is an increased Al/Si ratio of 0.47 compared to 0.30 to 0.39 in the other samples. In Raman spectra, Al-O-Si bonds fall in the range of Si-NBO [66, 67]. Aluminate stretching is reported to be weak compared to Si-O stretching so that the presence of aluminate bands is likely masked by silicate bands [30, 31, 60]. However, the presence of a weak Al-O-Si band can lead to an overestimation of NBO. The increased Al/Si ratio in GGBS14 thus might explain the difference from the regression line of the other samples. This illustrates that large variations in the Al/Si ratios of a glass limit the application of Raman spectra to detect variations in the degree of Si network polymerization.

Besides tetrahedron connectivity, the relative intensity of the Si-O bands is also influenced by the field strength of the compensation cation [31]. In slag glasses, the compensating cation are

mainly Ca and Mg. The substitution of Ca by Mg was reported to only slightly change Raman spectra of glasses, so that this influence can be excluded [33].

4.3 Description of the vitreous network of slag based on NMR data

All ^{27}Al NMR spectra showed unambiguously that Al atoms are in a large majority four-fold coordinated to oxygen and contribute to the network polymerization. Moreover, AlO_4^- tetrahedra bind the alkaline cations and a part of the alkaline earth cations for their charge compensation, as indicated by the value of quadrupolar coupling constants ($C_Q \approx 8$ kHz) [36, 45]. The quantity of alkaline earth cations responsible of network depolymerisation (NBO formation) is thereby reduced. Finally, the high ^{27}Al chemical shift indicates the presence of NBO in the Al tetrahedral units, as would be expected for a depolymerized glass structure [30, 36]. The presence of Al_V, although weak (between 2 and 8%), could indicate some inhomogeneities in the vitreous network. Five-fold coordinated Al is generally observed in peraluminous glasses, i.e., when the amount of cations is not able to charge-balance all AlO_4^- so that electrical neutrality is achieved by a change in Al coordination [36]. Therefore, Al_V could be the sign of the presence of rich-aluminum domains.

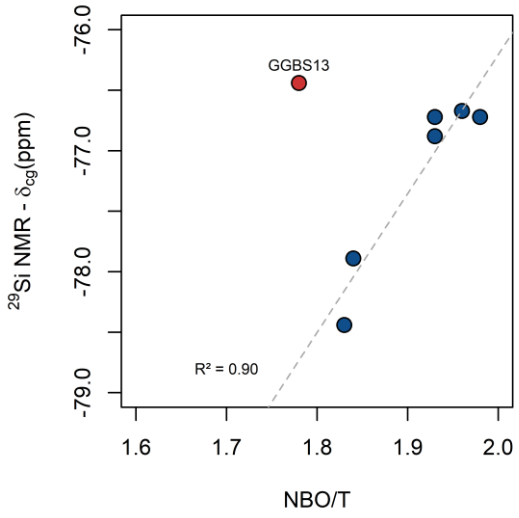

Figure 5. ^{29}Si NMR δ_{CG} plotted against theoretical NBO/T. The dotted line represents a linear regression, excluding GGBS13.

In the complex case of industrial slags, the quantitative deconvolution of ^{29}Si NMR spectra is impossible because of the wide variety of silicon environments and the absence of discontinuities on the signal. The ^{29}Si NMR δ_{CG} and NBO/T follow the same trend (Figure 5). Linear regression between NBO/T and ^{29}Si NMR δ_{CG} ratios gave an R^2 of 0.90 if the value measured on GGBS13 is omitted, as it is tainted with paramagnetic effect. However, the ^{29}Si chemical shift depends on many parameters in our systems. First, the bridging or non-bridging nature of the first coordination sphere oxygen atoms, defining the Q^n units [68]. All other things being equal, the breaking of an O-Si bond per tetrahedron induces a positive shift of 10 ppm [69]. Second, the substitution of a Si atom by an Al atom in the second sphere of coordination defining the Q^n(mAl) induces a positive shift of 5 ppm [69], and third there is also an effect depending on the nature of the counter ions (alkaline or alkaline earth). To these main effects are added smaller shifts due to variations in angles and distances present in disordered networks [70]. Based on these considerations, the difference of the center of gravities (δ_{CG}) will be interpreted with respect to the two most influencing parameters: estimated NBO/T and Al/Si. Figure 6 represents δ_{CG}, FWHM, NBO/T and Al/Si ratio for our GGBS samples.

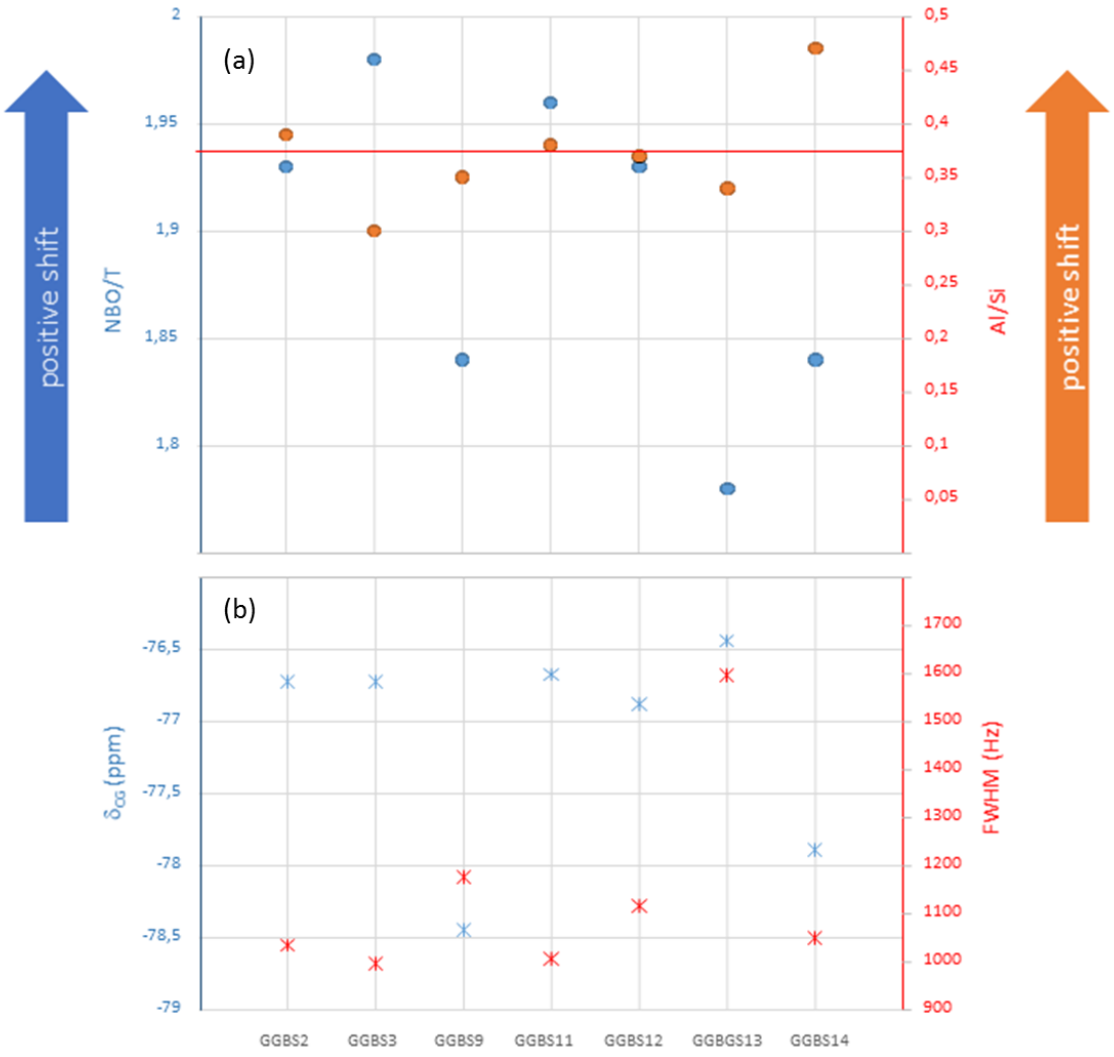

Figure 6. (a) Estimated NBO/T values from composition and Al/Si molar ratios of the different GGBS. (b) Gravity center and FWHM values from NMR analysis of the different GGBS. The red line corresponds to the mean effect observed for GGBS2 that was consider here as the reference.

For our analyses, GGBS2 was arbitrary considered as the reference system. δ_{CG} of GGBS3 is almost the same, due to two opposite effects: a negative shift due to lower Al/Si ratio implying a lower probability of the Si-O-Al bond, opposed to a positive shift because of higher estimated NBO/T. As a result, the GGBS3 network is less polymerized than that of GGBS2, contrary to what the position of the peak suggests. In the case of GGBS11 and GGBS12, the two effects are small and do almost completely compensate, it can be assumed that the degree of

polymerization of GGBS2, GGBS11 and GGBS12 are equivalent. In the case of GGBS9, both Al/Si and NBO/T are lower, inducing a negative shift. This explains the low measured δ_{CG} and proves the higher degree of polymerization of the glass network. The situation should be the same for GGBS13, however the measured δ_{CG} is close to that of GGBS2. This can probably be attributed to the paramagnetic interaction and confirms that NMR is not suitable for analysis of samples that contain > 1 wt.% of paramagnetic metal oxides. Finally, in the case of GGBS14, the higher Al/Si induces a positive shift opposite to the negative shift due to lower NBO/T. The more negative δ_{CG} measured for GGBS14 is due to the higher effect of NBO/T and is coherent with a more polymerized network. The samples could then be ordered as followed GGBS3<GGBS2≈GGBS11≈GGBS12<GGBS14<GGBS9 from the less to the more polymerized alumino-silicate network.

4.4 Comparison of Raman and NMR spectroscopic results

Both spectroscopies gave data in line with theoretic NBO/T calculations. Therefore, we can state that there is no major derivation from known structural behaviors of main components in complex industrial slag glasses. However, the presence of a multitude of elements complicated spectroscopic analysis.

Luminescence effects overprinted traditional Raman signals. Time resolved Raman analysis allowed the acquisition of exploitable spectra, by circumventing luminescence effects, highlighting a potential application of this still rare technique. Spectra deconvolution was straightforward and gave a good first impression of the glass structure, especially as the acquisition time is low, in the order of minutes. However, the Raman signal of Si tetrahedra is superposed with a much weaker Al tetrahedron signal, that can false the interpretation if large variations of Al are present. A major drawback of Raman analysis is that it is complicated to fit the Raman bands of Al, the bands entirely overlap with the Si signals.

^{27}Al NMR can conveniently investigate the Al environment in complex glasses, except in presence of high amount of paramagnetic nuclei. The coordination state can be determined and quantified from those spectra. Acquisition times for ^{27}Al spectra was in the order of 1 hour.

Due to the low natural abundance of ^{29}Si (4.7%), the acquisition of ^{29}Si MAS spectra of our selected glass takes at least 24 h. ^{29}Si chemical shift is sensitive to the composition of its second coordination sphere. Each environment induces a specific chemical shift in the range of -70 to -110 ppm. In the case of our slags, the multitude of possible silicon environments and the absence of discontinuities on the signal make spectra deconvolution impossible. Still the center of gravity of ^{29}Si NMR spectra can be used to derive a rough impression of the polymerization degree of Si in complex glasses, especially for compositions with Al/Si ratio almost constant. As for ^{27}Al spectra, the quality of ^{29}Si spectra might be reduced by paramagnetic effects.

The degree of polymerization of the slag glasses derived from Raman spectroscopy, NMR spectroscopy and theoretical NBO/T calculations, did not directly correlate with the reactivity reported in [12].This indicates that the glass structure, that is strongly linked to the dissolution rate of glasses, is not the only controlling factor of GGBS reactivity [20]. That is likely due to (1) the influence of the solution composition on dissolution rate [71] and (2) the differences in solution and hydrate stoichiometry that represent a supplementary control reactivity [12].

4. Conclusion

GGBS are glass by-products from pig iron production commonly used as supplementary cementitious materials in blended cements. In this study, experimental determination of their degree of glass network polymerization was attempted in order to contribute to the understanding of GGBS reactivity in blended cements. Based on composition and electroneutrality considerations, it is possible to estimate the degree of polymerization of vitreous GGBS network (NBO/T). This simplistic calculation gives a rapid, global view of the network, but is based on various hypotheses as the structural role of the different elements, the equivalent repartition of NBO on the tetrahedral and the structural homogeneity of the material.

Raman and NMR spectroscopies are widely used for structural characterization of glasses; however, they face difficulties in the case of industrial slag, containing a multitude of different elements. Traditional continuous Raman spectra of the GGBS are overprinted by strong luminescence effects for exciting wavelength of 355, 514, 633 and 785 nm, likely due to the presence of 3d transition-metals in the slag glasses (Sc to Cu). Time-resolved Raman analysis effectively eliminated the luminescence and allowed very fast acquisition (~1 min) of exploitable spectra for all industrial GGBS. Solid state NMR spectra acquisition are possible for all samples. However, ^{29}Si NMR spectra, the most informative data for polymerization description necessitated at least 24h hours of acquisition and a rigorous signal treatment. For both Raman and NMR spectra, the deconvolution is tricky, even if a correlation of NBO/T with Raman Q_0/Q_2 area and ^{29}Si δ_{CG} NMR could follow an acceptable linear regression. However, both techniques underline that a rigorous interpretation of spectral data should take into account the presence of Al-O-Si bounds.

Acknowledgements

This project has received funding from the Research Fund for Coal and Steel under grant agreement No 749809 (Actislag). The Renishaw Invia spectrometers were funded by the EquipeX PlaneX ANR-11-EQPX-36

5. References

1. Matthes W, Vollpracht A, Villagrán Y, et al (2018) Ground Granulated Blast-Furnace Slag. In: De Belie N, Soutsos M, Gruyaert E (eds) Properties of Fresh and Hardened Concrete Containing Supplementary Cementitious Materials. Springer International Publishing, Cham, pp 1–53

2. Smolczyk H-G (1980) Structure des laitiers et hydratation des ciments de laitiers : structure et caractérisation des laitiers. In: RAPPORTS PRINCIPAUX. Paris, p III-1/1-1/17

3. Taylor HFW (1997) Cement chemistry, 2nd ed. Thomas Telford Publishing

4. Schröder F (1969) Slags and slag cements. In: Proceedings of the 5th international symposium on the chemistry of cement. Tokyo, pp 149–199

5. Bijen J (1996) Benefits of slag and fly ash. Constr Build Mater 10:309–314. https://doi.org/10.1016/0950-0618(95)00014-3

6. Ehrenberg A (2002) CO2 emissions and energy consumption of granulated blastfurnace slag. In: Proceedings Manufacturing and Processing of Iron and Steel Slags. Euroslag publication, Keyworth, UK, pp 151–166

7. Hogan F, Meusel J (1981) Evaluation for Durability and Strength Development of a Ground Granulated Blast Furnace Slag. Cem Concr Aggreg 3:40. https://doi.org/10.1520/CCA10201J

8. Van den Heede P, De Belie N (2012) Environmental impact and life cycle assessment (LCA) of traditional and 'green' concretes: Literature review and theoretical calculations. Cem Concr Compos 34:431–442. https://doi.org/10.1016/j.cemconcomp.2012.01.004

9. Ehrenberg A, Israel D, Kühn A, et al (2008) Hüttensand: Reaktionspotenzial und Herstellung optimierter Zemente Tl.1 (Granulated blast furnace slag: reaction potential and production of optimized cements, part 1). Cem Int

10. Robeyst N, Gruyaert E, Grosse CU, De Belie N (2008) Monitoring the setting of concrete containing blast-furnace slag by measuring the ultrasonic p-wave velocity. Cem Concr Res 38:1169–1176. https://doi.org/10.1016/j.cemconres.2008.04.006

11. Smolczyk H-G (1978) Zum Einfluß der Chemie des Hüttensands auf die Festigkeit von Hochofenzementen. Zem. - Kalk - Gips 294–296

12. Blotevogel S, Ehrenberg A, Steger L, et al (2020) Ability of the R3 test to evaluate differences in early age reactivity of 16 industrial ground granulated blast furnace slags (GGBS). Cem Concr Res 130:105998. https://doi.org/10.1016/j.cemconres.2020.105998

13. Blotevogel S, Steger L, Hart D, et al (2020) Effect of TiO_2 and 10 minor elements on the reactivity of ground granulated blast furnace slag (GGBS) in blended cements. J Am Ceram Soc jace.17431. https://doi.org/10.1111/jace.17431

14. Ben Haha M, Lothenbach B, Le Saout G, Winnefeld F (2012) Influence of slag chemistry on the hydration of alkali-activated blast-furnace slag — Part II: Effect of Al2O3. Cem Concr Res 42:74–83. https://doi.org/10.1016/j.cemconres.2011.08.005

15. Ben Haha M, Lothenbach B, Le Saout G, Winnefeld F (2011) Influence of slag chemistry on the hydration of alkali-activated blast-furnace slag — Part I: Effect of MgO. Cem Concr Res 41:955–963. https://doi.org/10.1016/j.cemconres.2011.05.002

16. Gong K, White CE (2016) Impact of chemical variability of ground granulated blast-furnace slag on the phase formation in alkali-activated slag pastes. Cem Concr Res 89:310–319. https://doi.org/10.1016/j.cemconres.2016.09.003

17. Tänzer R, Buchwald A, Stephan D (2015) Effect of slag chemistry on the hydration of alkali-activated blast-furnace slag. Mater Struct 48:629–641. https://doi.org/10.1617/s11527-014-0461-x

18. Wang PZ, Trettin R, Rudert V, Spaniol T (2004) Influence of Al_2O_3 content on hydraulic reactivity of granulated blast-furnace slag, and the interaction between Al_2O_3 and CaO. Adv Cem Res 16:1–7. https://doi.org/10.1680/adcr.2004.16.1.1

19. Whittaker M, Zajac M, Ben Haha M, et al (2014) The role of the alumina content of slag, plus the presence of additional sulfate on the hydration and microstructure of Portland cement-slag blends. Cem Concr Res 66:91–101. https://doi.org/10.1016/j.cemconres.2014.07.018

20. Bunker BC (1994) Molecular mechanisms for corrosion of silica and silicate glasses. J Non-Cryst Solids 179:300–308. https://doi.org/10.1016/0022-3093(94)90708-0

21. Shimoda K, Tobu Y, Kanehashi K, et al (2008) Total understanding of the local structures of an amorphous slag: Perspective from multi-nuclear (29Si, 27Al, 17O, 25Mg, and 43Ca) solid-state NMR. J Non-Cryst Solids 354:1036–1043. https://doi.org/10.1016/j.jnoncrysol.2007.08.010

22. Huang C, Behrman EC (1991) Structure and properties of calcium aluminosilicate glasses. J Non-Cryst Solids 128:310–321. https://doi.org/10.1016/0022-3093(91)90468-L

23. Li C, Sun HH, Li LT (2010) Glass Phase Structure of Blast Furnace Slag. Adv Mater Res 168–170:3–7. https://doi.org/10.4028/www.scientific.net/AMR.168-170.3

24. Risbud SH, Kirkpatrick RJ, Taglialavore AP, Montez B (1987) Solid-state NMR Evidence of 4-, 5, and 6-Fold Aluminum Sites in Roller-Quenched SiO2-A12O3 Glasses. J Am Ceram Soc 70:C-10-C–12. https://doi.org/10.1111/j.1151-2916.1987.tb04859.x

25. Toplis MJ, Kohn SC, Smith ME, Poplett IJF (2000) Fivefold-coordinated aluminum in tectosilicate glasses observed by triple quantum MAS NMR. Am Mineral 85:1556–1560. https://doi.org/10.2138/am-2000-1031

26. Sen S, Youngman RE (2004) High-Resolution Multinuclear NMR Structural Study of Binary Aluminosilicate and Other Related Glasses. J Phys Chem B 108:7557–7564. https://doi.org/10.1021/jp031348u

27. Neuville DR, Cormier L, Flank A-M, et al (2004) Al speciation and Ca environment in calcium aluminosilicate glasses and crystals by Al and Ca K-edge X-ray absorption spectroscopy. Chem Geol 213:153–163. https://doi.org/10.1016/j.chemgeo.2004.08.039

28. Lee S, Min DJ (2018) Investigation of sulfide capacity of aluminosilicate slag based on ionic structure considerations. J Am Ceram Soc 101:634–643. https://doi.org/10.1111/jace.15227

29. Le Cornec D, Cormier L, Galoisy L, et al (2021) Molecular structure of amorphous slags: An experimental and numerical approach. J Non-Cryst Solids 556:120444. https://doi.org/10.1016/j.jnoncrysol.2020.120444

30. Neuville DR, Cormier L, Montouillout V, et al (2008) Amorphous materials: Properties, structure, and durability: Structure of Mg- and Mg/Ca aluminosilicate glasses: 27Al NMR and Raman spectroscopy investigations. Am Mineral 93:1721–1731. https://doi.org/10.2138/am.2008.2867

31. McMillan P, Piriou B, Navrotsky A (1982) A Raman spectroscopic study of glasses along the joins silica-calcium aluminate, silica-sodium aluminate, and silica-potassium aluminate. Geochim Cosmochim Acta 46:2021–2037. https://doi.org/10.1016/0016-7037(82)90182-X

32. McMillan P, Piriou B (1983) Raman spectroscopy of calcium aluminate glasses and crystals. J Non-Cryst Solids 55:221–242. https://doi.org/10.1016/0022-3093(83)90672-5

33. Merzbacher CI, White WB (1991) The structure of alkaline earth aluminosilicate glasses as determined by vibrational spectroscopy. J Non-Cryst Solids 130:18–34. https://doi.org/10.1016/0022-3093(91)90152-V

34. Mysen B, Neuville D (1995) Effect of temperature and TiO2 content on the structure of Na2Si2O5Na2Ti2O5 melts and glasses. Geochim Cosmochim Acta 59:325–342. https://doi.org/10.1016/0016-7037(94)00290-3

35. Neuville DR, Mysen BO (1996) Role of aluminium in the silicate network: In situ, high-temperature study of glasses and melts on the join SiO2-NaAlO2. Geochim Cosmochim Acta 60:1727–1737. https://doi.org/10.1016/0016-7037(96)00049-X

36. Neuville DR, Cormier L, Massiot D (2006) Al coordination and speciation in calcium aluminosilicate glasses: Effects of composition determined by 27Al MQ-MAS NMR and Raman spectroscopy. Chem Geol 229:173–185. https://doi.org/10.1016/j.chemgeo.2006.01.019

37. Kucharczyk S, Sitarz M, Zajac M, Deja J (2018) The effect of CaO/SiO 2 molar ratio of CaO-Al 2 O 3 - SiO 2 glasses on their structure and reactivity in alkali activated system. Spectrochim Acta A Mol Biomol Spectrosc 194:163–171. https://doi.org/10.1016/j.saa.2018.01.018

38. Liang D, Yan Z, Lv X, et al (2017) Transition of Blast Furnace Slag from Silicate-Based to Aluminate-Based: Structure Evolution by Molecular Dynamics Simulation and Raman Spectroscopy. Metall Mater Trans B 48:573–581. https://doi.org/10.1007/s11663-016-0855-y

39. Zheng K, Liao J, Wang X, Zhang Z (2013) Raman spectroscopic study of the structural properties of CaO–MgO–SiO2–TiO2 slags. J Non-Cryst Solids 376:209–215. https://doi.org/10.1016/j.jnoncrysol.2013.06.003

40. Keeley PM, Rowson NA, Johnson TP, Deegan DE (2017) The effect of the extent of polymerisation of a slag structure on the strength of alkali-activated slag binders. Int J Miner Process 164:37–44. https://doi.org/10.1016/j.minpro.2017.05.007

41. Raffaëlly L, Champagnon B (2007) High temperature experiments: a way to observe Raman scattering in luminescent samples. J Raman Spectrosc 38:1242–1245. https://doi.org/10.1002/jrs.1757

42. Fotso Gueutue ES, Canizares A, Simon P, et al (2018) Nanosecond time-resolved Raman spectroscopy for solving some Raman problems such as luminescence or thermal emission. J Raman Spectrosc 49:822–829. https://doi.org/10.1002/jrs.5345

43. Tobon YA, Bormann D, Canizares A, et al (2011) Time-resolved Raman studies on $Al_2O_3:Cr^{3+}$: lifetime measurements of the excited-state transition $\bar{E} \rightarrow 2\bar{A}$. J Raman Spectrosc 42:1109–1113. https://doi.org/10.1002/jrs.2834

44. Charpentier T, Okhotnikov K, Novikov AN, et al (2018) Structure of Strontium Aluminosilicate Glasses from Molecular Dynamics Simulation, Neutron Diffraction, and Nuclear Magnetic Resonance Studies. J Phys Chem B 122:9567–9583. https://doi.org/10.1021/acs.jpcb.8b05721

45. Florian P, Sadiki N, Massiot D, Coutures JP (2007) ^{27}Al NMR Study of the Structure of Lanthanum- and Yttrium-Based Aluminosilicate Glasses and Melts. J Phys Chem B 111:9747–9757. https://doi.org/10.1021/jp072061q

46. Dutreilh-Colas M, Canizares A, Blin A, et al (2011) In Situ Raman Diagnostic of Structural Relaxation Times of Silica Glasses: In Situ Raman Diagnostic of Silica Glasses. J Am Ceram Soc 94:2087–2091. https://doi.org/10.1111/j.1551-2916.2011.04426.x

47. McMillan P (1984) A Raman spectroscopics tudy of glasses in the system CaO-MgO-SiO2. Am Mineral 69:645–659

48. Helmus JJ, Jaroniec CP (2013) Nmrglue: an open source Python package for the analysis of multidimensional NMR data. J Biomol NMR 55:355–367. https://doi.org/10.1007/s10858-013-9718-x

49. Harris CR, Millman KJ, van der Walt SJ, et al (2020) Array programming with NumPy. Nature 585:357–362. https://doi.org/10.1038/s41586-020-2649-2

50. Massiot D, Fayon F, Capron M, et al (2002) Modelling one- and two-dimensional solid-state NMR spectra: Modelling 1D and 2D solid-state NMR spectra. Magn Reson Chem 40:70–76. https://doi.org/10.1002/mrc.984

51. Czjzek G, Fink J, Götz F, et al (1981) Atomic coordination and the distribution of electric field gradients in amorphous solids. Phys Rev B 23:2513–2530. https://doi.org/10.1103/PhysRevB.23.2513

52. Mysen BO, Virgo D, Scarfe CM (1980) Relations between the anionic structure and viscosity of silicate melts-a Raman spectroscopic study. Am Mineral 65:690–710

53. Le Losq C, Neuville DR, Florian P, et al (2014) The role of Al3+ on rheology and structural changes in sodium silicate and aluminosilicate glasses and melts. Geochim Cosmochim Acta 126:495–517. https://doi.org/10.1016/j.gca.2013.11.010

54. Kalampounias AG, Yannopoulos SN, Papatheodorou GN (2006) A high-temperature Raman spectroscopic investigation of the potassium tetrasilicate in glassy, supercooled, and liquid states. J Chem Phys 125:164502. https://doi.org/10.1063/1.2360275

55. McMillan PF, Poe BT, Gillet PH, Reynard B (1994) A study of SiO2 glass and supercooled liquid to 1950 K via high-temperature Raman spectroscopy. Geochim Cosmochim Acta 58:3653–3664. https://doi.org/10.1016/0016-7037(94)90156-2

56. Mysen BO, Virgo D, Seifert FA (1982) The structure of silicate melts: Implications for chemical and physical properties of natural magma. Rev Geophys 20:353. https://doi.org/10.1029/RG020i003p00353

57. Bechgaard TK, Scannell G, Huang L, et al (2017) Structure of MgO/CaO sodium aluminosilicate glasses: Raman spectroscopy study. J Non-Cryst Solids 470:145–151. https://doi.org/10.1016/j.jnoncrysol.2017.05.014

58. Nesbitt HW, Henderson GS, Bancroft GM, Neuville DR (2021) Spectral Resolution and Raman Q3 and Q2 cross sections in ~40 mol% Na2O glasses. Chem Geol 562:120040. https://doi.org/10.1016/j.chemgeo.2020.120040

59. Zheng K, Liao J, Wang X, Zhang Z (2013) Raman spectroscopic study of the structural properties of CaO–MgO–SiO2–TiO2 slags. J Non-Cryst Solids 376:209–215. https://doi.org/10.1016/j.jnoncrysol.2013.06.003

60. McMillan P, Piriou B (1982) The structures and vibrational spectra of crystals and glasses in the silica-alumina system. J Non-Cryst Solids 53:279–298. https://doi.org/10.1016/0022-3093(82)90086-2

61. Engelhardt G (1989) Multinuclear solid-state NMR in silicate and zeolite chemistry. TrAC Trends Anal Chem 8:343–347. https://doi.org/10.1016/0165-9936(89)87043-8

62. Neuville DR, Cormier L, Massiot D (2004) Al environment in tectosilicate and peraluminous glasses: A 27Al MQ-MAS NMR, Raman, and XANES investigation. Geochim Cosmochim Acta 68:5071–5079. https://doi.org/10.1016/j.gca.2004.05.048

63. Brown GE, Farges F, Calas G (1995) X-Ray Scattering and X-Ray Spectroscopy Studies of Silicate Melts. In: Rev. Mineral. Mineralogical Society of America, Washington D.C., pp 317–410

64. Stebbins JF (1995) Chapter 7. DYNAMICS AND STRUCTURE OF SILICATE AND OXIDE MELTS: NUCLEAR MAGNETIC RESONANCE STUDIES. In: Stebbins JF, McMillan PF, Dingwell DB (eds). De Gruyter, pp 191–246

65. Le Cornec D, Galoisy L, Izoret L, et al (2021) Structural role of titanium on slag properties. J Am Ceram Soc 104:105–113. https://doi.org/10.1111/jace.17407

66. McMillan P, Piriou B, Navrotsky A (1982) A Raman spectroscopic study of glasses along the joins silica-calcium aluminate, silica-sodium aluminate, and silica-potassium aluminate. Geochim Cosmochim Acta 46:2021–2037. https://doi.org/10.1016/0016-7037(82)90182-X

67. McMillan P, Piriou B (1982) The structures and vibrational spectra of crystals and glasses in the silica-alumina system. J Non-Cryst Solids 53:279–298. https://doi.org/10.1016/0022-3093(82)90086-2

68. Lippmaa E, Maegi M+, Samoson A, et al (1980) Structural studies of silicates by solid-state high-resolution silicon-29 NMR. J Am Chem Soc 102:4889–4893

69. Lippmaa E, Maegi M+, Samoson A, et al (1981) Investigation of the structure of zeolites by solid-state high-resolution silicon-29 NMR spectroscopy. J Am Chem Soc 103:4992–4996

70. Hiet J, Deschamps M, Pellerin N, et al (2009) Probing chemical disorder in glasses using silicon-29 NMR spectral editing. Phys Chem Chem Phys 11:6935–6940

71. Snellings R (2013) Solution-Controlled Dissolution of Supplementary Cementitious Material Glasses at pH 13: The Effect of Solution Composition on Glass Dissolution Rates. J Am Ceram Soc 96:2467–2475. https://doi.org/10.1111/jace.12480